SERI/TP-217-3433
UC Category: 261
DE89000854

Aerodynamic Pressure and Flow-Visualization Measurement from a Rotating Wind Turbine Blade

C. P. Butterfield

November 1988

Prepared for the Eighth ASME
Wind Energy Symposium
Houston, Texas
22-25 January 1989

Prepared under Task No. WE811001

Solar Energy Research Institute
A Division of Midwest Research Institute

1617 Cole Boulevard
Golden, Colorado 80401-3393

Prepared for the
U.S. Department of Energy
Contract No. DE-AC02-83CH10093

NOTICE

Printed in the United States of America
Available from:
National Technical Information Service
U.S. Department of Commerce
5285 Port Royal Road
Springfield, VA 22161

Price: Microfiche A01
Printed Copy A02

Codes are used for pricing all publications. The code is determined by the number of pages in the publication. Information pertaining to the pricing codes can be found in the current issue of the following publications which are generally available in most libraries: *Energy Research Abstracts (ERA)*; *Government Reports Announcements* and Index (*GRA* and I); *Scientific and Technical Abstract Reports (STAR)*; and publication NTIS-PR-360 available from NTIS at the above address.

AERODYNAMIC PRESSURE AND FLOW-VISUALIZATION MEASUREMENT FROM A ROTATING WIND TURBINE BLADE

C.P. Butterfield

Solar Energy Research Institute
Golden, CO 80401

ABSTRACT

Aerodynamic, load, flow-visualization, and inflow measurements have been made on a 10-m, three-bladed, downwind, horizontal-axis wind turbine (HAWT). A video camera mounted on the rotor was used to record nighttime and daytime video images of tufts attached to the low-pressure side of a constant-chord, zero-twist blade. Load measurements were made using strain gages mounted at every 10% of the blade's span. Pressure measurements were made at 80% of the blade's span. Pressure taps were located at 32 chordwise positions, revealing pressure distributions comparable with wind tunnel data. Inflow was measured using a vertical-plane array of eight propvane and five triaxial (U-V-W) prop-type anemometers located 10 m upwind in the predominant wind direction.

One objective of this comprehensive research program was to study the effects of blade rotation on aerodynamic behavior below, near, and beyond stall. To this end, flow patterns are presented here that reveal the dynamic and steady behavior of flow conditions on the blade. Pressure distributions are compared to flow patterns and two-dimensional wind tunnel data. Separation boundary locations are shown that change as a function of spanwise location, pitch angle, and wind speed.

INTRODUCTION

The analyses of HAWT aerodynamics assume that blade spanwise sections can be treated as independent airfoils operating in a two-dimensional, wind-tunnel-like flow condition. This assumption implies that there is no exchange of momentum in the spanwise direction. This has proven to be a reasonable assumption for HAWTs operating at medium to high tip-speed ratios. Even helicopters, which operate in a highly three-dimensional flow state, can be analyzed using two-dimensional airfoil data.

However, when stall occurs on a rotating HAWT blade, analytical predictions break down. In high winds, HAWTs actually produce more power and experience higher loads than standard analyses would predict using two-dimensional wind tunnel data. This unexplained increase in performance appears to be a steady-state phenomenon that researchers have called "delayed stall." Dynamic blade loads measured on HAWTs have been larger than predicted using existing aeroelastic analysis. This problem may be caused by inaccurate modeling of complex inflow to the rotor. These analyses are typically capable of modeling simple wind shear and in some codes even complex steady-state wind shear. But even the complex model may not be accurate enough because it assumes a steady shear when actually the inflow is turbulent (i.e., constantly changing).

This may or may not be the explanation for the poor prediction of dynamic loads; certainly it is a contributor, but there may be other contributors, such as dynamic stall or spanwise flow. Both dynamic stall and spanwise flow have contributed to increasing loads on helicopter rotors. Engineers in the helicopter industry had to make detailed pressure measurements on blades and flow-visualization measurements before they were able to understand the complex fluid dynamic processes that caused these loads. The same is true for HAWTs. Results of this program will help determine (1) if aerodynamic forces are obeying two-dimensional airfoil characteristics, (2) how turbulent inflow must be transformed into a rotational frame of reference, and (3) if lift coefficients are reaching levels higher than those possible in two-dimensional flow. Pressure and flow-visualization measurements are the essential first step that must be taken before dynamic stall, spanwise flow, delayed stall, or other three-dimensional flow phenomena can be isolated. Once the dominant physical process is isolated, subsequent detailed test programs can focus on understanding and modifying it.

The test program described in this report was funded by the Department of Energy (DOE) and conducted by the Solar Energy Research Institute (SERI) at its Wind Energy Test Center (WETC) in Golden, Colo. This test, called the "Combined Experiment," includes all the essential physical measurements mentioned above. Flow patterns were recorded using a high-speed video camera mounted on the rotor to view small tufts mounted on the blade. Pressure transducers and angle-of-attack (AOA) probes were also used to measure lift coefficients and corresponding angles of attack. Finally, detailed, near-field inflow measurements and blade-load measurements were made simultaneously. These data will

provide researchers with a comprehensive picture of the inflow profile, how that inflow affects aerodynamic loads, and how these aerodynamic loads correlate with structural loads. Results shown in this report were produced by preliminary data analyses. The test is still in progress and is expected to continue through the spring of 1989. This report is intended to be an overview of preliminary data and not a comprehensive analysis of any results to date. Future reports will deal comprehensively with various topics.

OBJECTIVES

The major objectives of the test are to understand the complete, local flow field acting on a rotating wind turbine blade. Specific questions include the following:

1. Do airfoil pressure distributions measured on a rotating blade differ from those measured in the wind tunnel at angles of attack (a) below stall and (b) above stall?
2. Is there radial flow near or in the boundary layer of the airfoil that affects pressure distributions (a) below stall and (b) above stall?
3. Is there evidence of dynamic stall that could result in increased dynamic loads?
4. Does the separation boundary location measured on the rotating blade agree with that measured in two-dimensional flow in the wind tunnel?

The answers to these questions will result from a close examination of pressure distributions and flow direction patterns measured on a rotating wind turbine, and from a comparison of these measurements with wind tunnel data. The experiment will provide a "reference data set" for validation of aerodynamic, structural, and fatigue models by carefully measuring atmospheric pressure distributions on the airfoil and determining machine responses to these loads.

TEST SETUP

The Grumman Wind Stream 33 was used as the test turbine. Figures 1 and 2 show the turbine's original characteristics. This turbine was an excellent test turbine for the Combined Experiment for the following reasons:

1. The rigid, three-bladed hub reduced the possibility of blade motion affecting the data.
2. A constant-chord, zero-twist, zero-thickness taper blade was used, thus reducing the effects of blade geometry on stalled flow (because stalled characteristics can be affected by twist and thickness taper).
3. The Wind Stream 33 was a downwind machine. This allowed a camera to be mounted on a boom extending downwind and aimed at the low-pressure side of the blade, so that tufts mounted on the blade could be viewed easily.
4. The machine and tower lent themselves to the modifications needed for the test, such as tilting the tower, mounting the transducer, and modifying the control system.
5. The pitch control system allowed variations in stall or AOA for any wind speed.

Significant modifications were made to the blade. Although the original blade planform was maintained (constant-chord, zero-twist, zero-taper), a new airfoil was selected. There were no wind tunnel data for the production airfoil, and wind tunnel data are crucial for comparisons between two-dimensional and three-dimensional pressure distributions.

The airfoil chosen was an S809 developed by Airfoils, Inc. under contract to SERI (1). This airfoil is well documented, including two-dimensional pressure

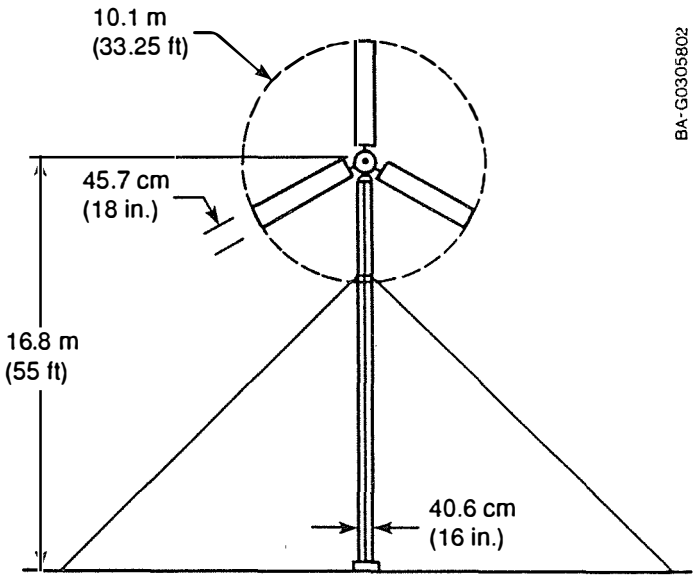

Windstream 33 Characteristics-

Induction generator rating	20 kW
Induction generator speed range	1800-1860 rpm
Gearbox ratio	25.1:1
Rotor speed	74.1 rpm
Rotor diameter	33.25 ft
Rotor solidity	0.0615
Blade chord	1.5 ft
Power coefficient, Max ($C_{P\ MAX}$)	0.38°
Tip speed ratio at $C_{P\ MAX}$	5.25°
Wind speed at $C_{P\ MAX}$	17.0 mph
System efficiency at $C_{P\ MAX}$	83%
Output power at VW = 24 mph	15 kW*
Rotor coning angle	3-1/2°
Razor/Nacelle assembly wt.	2,589 lb.
Drive axis height	55 ft
Tower section	16.0 in./0 dia, 3/8 in. wall
Guy base	80 ft

*Predicted

Fig. 1. Characteristics of the Grumman WS33 wind turbine

distributions, separation boundary locations, drag data, and flow-visualization data. The blade material is fiberglass composite, and the blades are designed to be as stiff as possible to limit blade deflections. The dynamics of the blade are tailored to avoid coalescence of rotor harmonics with flapwise, edgewise, and torsional natural frequencies. To minimize the possibility of aeroelastic instabilities, the mass and elastic axes are aligned with the aerodynamic axis. The instrumented blade was painted black to contrast the white tufts.

Strain gages were mounted at several spanwise locations on the blade so that bending-moment distributions could be measured. An AOA transducer was mounted on a strut off the leading edge of the blade. A multitap pressure transducer was mounted inside the fiberglass blade (Figure 3), and pressures were measured through 32 tubes leading from the 32-tap pressure transducer to the surface of the blade. Frequency-dependent distortions in the pressure measurements were corrected using the inverse transfer function (2).

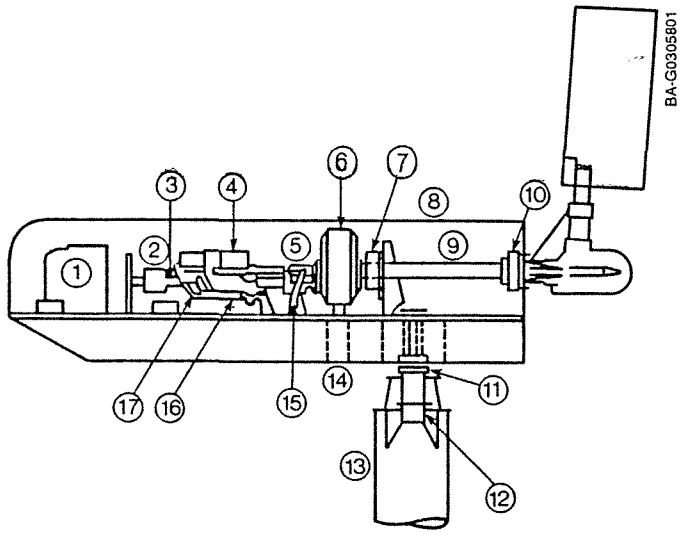

1 - Generator
2 - Disc brake
3 - H.S. shaft
4 - Pitch cont actuator
5 - Swivel
6 - Gear box
7 - Pillow block bearing
8 - Cowling
9 - Rotor shaft
10 - Flg block bearing
11 - Thrust bearing
12 - Vertical shaft
13 - Tower
14 - Strongback
15 - Torque link
16 - Redundant pitch cont actuator
17 - Redundant pitch actuator crank

Fig. 2. Schematic diagram of the Grumman WS33 wind turbine

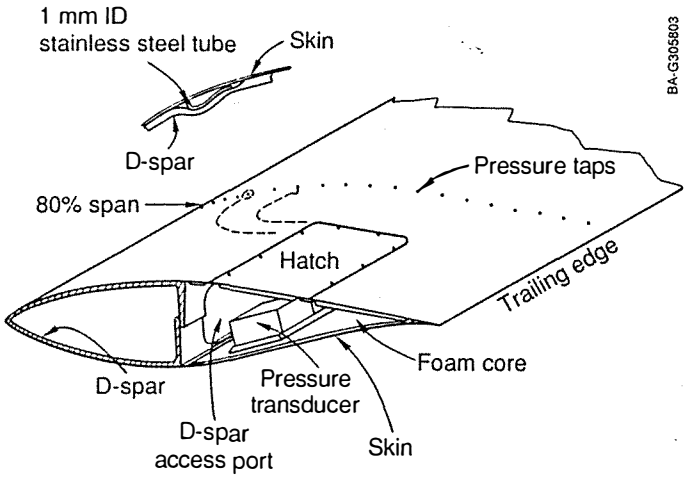

Fig. 3. Pressure transducer layout on the wind turbine blade

A guyed-pole tower was used with a hinged base and gin pole for easy tilt-down. An electric winch was used to lower and raise the system to aid in instrumentation checks and calibration. Careful attention was paid to tower and foundation loads when designing this system.

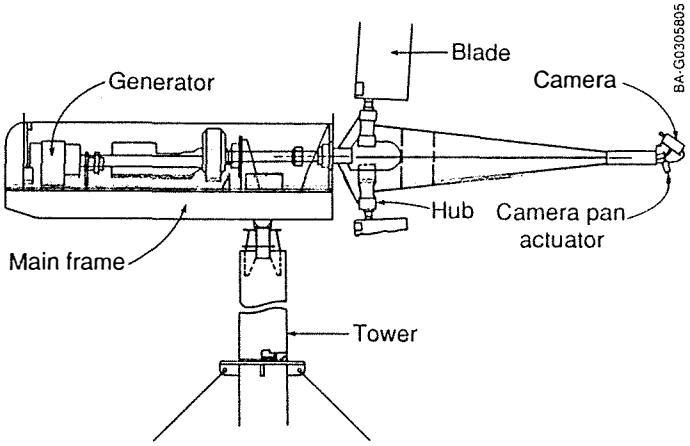

Fig. 4. Camera boom layout on the wind turbine

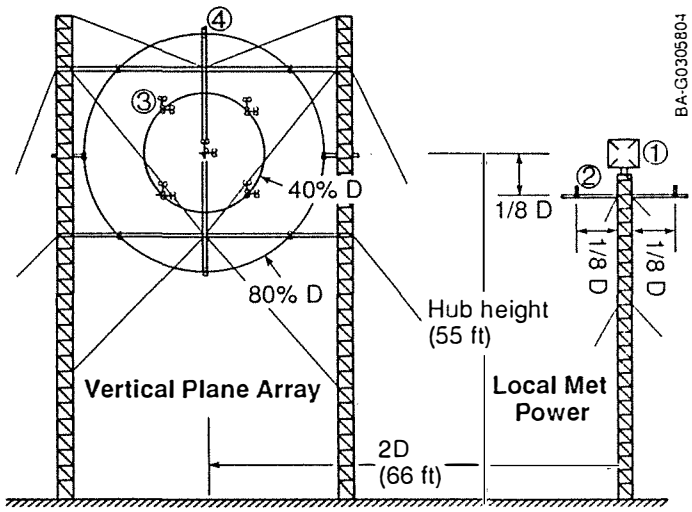

Item no.	Description
1	U-V-W sonic anemometer
2	Ruggedized TSI hot films
3	U-V-W gill anemometers
4	Prop vane anemometers

Fig. 5. Layout of the anemometers

A camera boom was designed to hold the 10-lb, high-shutter-speed video camera and was hinged at the base so that a complete tilt-down of the tower could be accomplished easily. It also has a system fundamental frequency of ten per revolution (10P). The boom was mounted on the hub and extended downwind 10 ft on the axis of rotation. This boom length allowed a view angle of 30° at the tip of the blade and 45° at the 66% span. Additional equipment was mounted on the boom, such as the data-acquisition system, the pressure system controller (PSC), and lighting for night testing (Figure 4).

A remote-controlled yaw lock was designed to allow various yaw positions to be set and released. This yaw retention system has a strain-gaged link to measure yaw moments.

Two Rohn 45G guyed meteorological (met) towers were placed to the west-northwest (290° direction) of the test machine (Figure 5). At the WETC, winds historically come from this direction in the spring. The two towers support three cross booms, where 13 anemometers

were mounted in a vertical-plane array to measure the inflow. The R.M. Young U-V-W anemometers measure three components of wind speed, have a bandwidth of DC to approximately 1 Hz, and were positioned one rotor diameter (1D) upwind of the turbine. Two TSI X-type hot-wire anemometers were placed near hub height on a third tower located just to the north of the vertical-plane array. The X-films provide measurements of horizontal and vertical wind velocity components at relatively high frequencies. Figure 5 shows the placement of these anemometers in a vertical-plane array, and also the placement of the two TSI X-wire anemometers and one triaxial sonic anemometer on the separate "local met tower."

INSTRUMENTATION

Tufts

The tufts consisted of 100% polyester white thread measuring approximately 0.25 mm in diameter and 45 mm in length ("mini tufts"). They were attached to the downwind side of the blade with super glue. Each row of tufts was spaced 76 mm from the next row in the blade spanwise direction. Ten tufts were placed in each row in the chordwise direction. This spacing resulted in approximately one tuft for every 10% of the chord in the chordwise direction, and one tuft every 1.5% of the span in the spanwise direction. The diameter of the tufts was chosen to minimize the effects on the boundary layer without making the tufts invisible to the video camera. Tufts that are large relative to the boundary layer thickness will cause transition and premature separation, which leads to a lower maximum lift coefficient ($C_{l,max}$). This effect is documented in (3).

Video Equipment

A NISUS N-2000 video camera was installed on a boom, and a recorder and monitor were placed in the control house so that the test engineer could observe the blade-mounted tufts and adjust the test according to the flow condition desired. The camera uses a mechanical shutter to freeze video frames in 1/625 of a second. Thirty video frames are recorded every second, which allows one frame to be recorded for every 11° of rotor azimuth position. The resolution of this system is limited by the standard 376 x 485 pixel density of the camera and recording system. For this reason, a close focus was needed to get a good angular measurement of the tufts. Various magnifications are used to maximize resolution and field of view. Information recorded on video tape is processed using video-image computer processing techniques.

Lighting

Night testing was necessary to avoid strain-gage thermal drift caused by uneven heating of the blade in sunlight. This resulted in the need for lighting to illuminate the white tufts for the video camera. Eleven 120-V spotlights were distributed along the camera boom and aimed at the blade, and they were focused along the outboard 50% of the blade span. The video pixel intensity of a tuft was 35 on a grey scale of 0 to 256, while the black background was 10 to 15; the contrast was great enough so that the tufts could be seen easily. Unfortunately, there was not enough light to operate the camera shutter, so moving images were blurred on the video display.

Angle-of-Attack Transducers

An accurate measurement of the blade AOA would be very useful in correlating wind tunnel data, analytical data, and test data. Unfortunately, this is also one of the most difficult measurements to make. Local flow is affected by the blade-induced velocity, which distorts measurements. Measuring the stagnation-point location has been used but has shown to produce erratic results. In wind tunnel tests, a wind vane has been used (4) that would align itself with the flow and indicate AOA. The vane was mounted on a probe attached to the blade. This approach has proven to be accurate (after analytical corrections), but reliability is a question. Sandia National Laboratories (SNL) attempted pressure sensing of the AOA with marginal success, but unsteady effects appeared to cause problems.

It was decided that the National Center for Atmospheric Research (NCAR) vane approach was best for the first attempt at measuring AOA. SERI developed a transducer based on the NCAR approach, with some improvements. This has been used during testing to measure AOA on the turbine blade with some success. Two problems have surfaced:

1. The vane is influenced by the local induced velocity.
2. The vane is slightly underdamped, causing a ringing of the vane.

In future testing, these problems will be corrected by

1. Making wind tunnel measurements of the induced velocity corrections and applying them to the measured data
2. Attempting analytical corrections of errors caused by induced velocity
3. Using an inverse transfer function to correct for the dynamic characteristics of the vane.

It is hoped that these corrections will improve the accuracy of the AOA measurements.

Pressure Measurements

Measuring pressure distributions on the rotating blade presented some problems. The pressures are typically less than 0.07 N/m^2, a bandwidth of 0-100 Hz was needed, and many channels must be measured in a small area of the blade surface without disturbing the surface contour. As mentioned earlier, the approach used was to mount a 32-tap ESP-32 pressure transducer inside the blade (Figure 3). Stainless-steel tubes less than 0.5 m in length were installed in the blade to carry surface pressures to the transducer. To document the dynamic effect of the tubes on measured pressures, transfer functions were measured between applied surface pressures and pressures measured by the transducer. Minimal distortion occurs below 50 Hz, but significant amplification occurs from 50 to 100 Hz. To compensate for this distortion, an inverse transfer function was used to correct the high-frequency pressure measurements. This technique is described in (2).

The ESP-32 pressure transducer made by PSI, Inc., was used because of its compact size and pressure sensitivity. Another advantage to using the ESP-32 pressure transducer is that it has a remote-control calibration capability. This allows the transducer to be calibrated while the turbine is rotating. It also makes it convenient to calibrate frequently to document any zero drift, which is common in some solid-state pressure transducers. SERI developed a control system for controlling the ESP-32 calibrations and conditioning the output signal to achieve a sample rate of 522 Hz per pressure tap. This system is used to perform calibrations every 5 min of test operation. The frequent calibration has resulted in data accurate to 2% (0.001 N/m^2) of the expected dynamic pressure.

The 32 pressure taps were located at 80% of full blade span, where the Reynolds number is approximately 10^6. The taps were lined up along the chord (instead of being staggered) so that spanwise variations in pressure distributions would not distort measured chordwise distributions. The chordwise spacing of the pressure taps was approximately logarithmic.

Anemometers

A variety of anemometers was used. The primary near-field measurements were all taken from anemometers mounted on the vertical-plane array and the near-field met tower (Figure 5). Additionally, far-field atmospheric stability measurements were taken at the test site's 50-m north met tower.

The vertical-plane array of R.M. Young three-axis prop anemometers provided low-frequency (0-1 Hz) windshear data, azimuthally varying wind data, and low-frequency inflow statistics. High-frequency (0-10 Hz) data were provided by a three-axis sonic anemometer mounted at hub height on the near-field met tower and two dual-axis hot-wire anemometers mounted 1.2 m below hub height.

Far-field atmospheric data were recorded from the north met tower. Data for temperature gradient (Richardson number), wind shear up to 50 m, and wind directions at four different altitudes were recorded from this tower.

Strain Gages

Strain gages were used to measure blade, tower, rotor, and yaw loads. Table 1 shows a complete list of the channels recorded. The rotor loads are listed under PCM-4 from channels 1 to 26. Blade flapwise and edgewise loads were measured at eight different spanwise locations. Pitching moment, or blade torsion, was measured at three spanwise locations. These load measurements were taken to establish reliable blade-load distributions to be used to confirm measured aerodynamic (applied) loads.

Each strain gage bridge was made up of four active gage elements mounted inside the fiberglass blade skin. The gages were located inside the skin instead of outside to preserve the accurate airfoil shape and surface smoothness.

Care was taken to position the strain gages to minimize flapwise and edgewise crosstalk. However, measurable crosstalk was discovered during the blade pull and strain-gage calibration tests. To eliminate this error, the crosstalk calibration coefficients were measured and used to correct the measured data.

A problem surfaced after the blades were mounted and the turbine was erected. The flat-black blade caused significant differential heating between the sunny and shady sides of the blade, thus inducing both apparent and real thermal strain in the gages on the sunny side but not on the shady side. Many techniques were considered to solve this problem, but the easiest to implement was testing at night, when both sides of the blade are nearly the same temperature. This minimized the zero drift but complicated the video recording of blade-mounted tufts. The long-term solution to this problem is painting the blade gloss white, which will be done for future testing.

Table 1. Instrumentation Channel Listing

North Met (PCM #6)

Ch	Parameter
01	20 M Hot Film
02	18 M Sonic U
03	18 M Sonic V
04	18 M Sonic W
05	5 M WD
06	5 M WS
07	10 M WD
08	10 M WS
09	20 M WD
10	20 M WS
11	50 M WD
12	50 M WS
13	5 M Air Temperature
14	Delta Temperature
15	5 M DP
16	Baro Pressure

VPA (PCM #2)

Ch	Parameter
01	VPA Anemometer WS-1
02	VPA Anemometer WS-2
03	VPA Anemometer WS-3
04	VPA Anemometer WS-4
05	VPA Anemometer WS-5
06	VPA Anemometer WS-6
07	VPA Anemometer WS-7
08	VPA Anemometer WS-8
09	VPA Anemometer WS-9U
10	VPA Anemometer WS-9V
11	VPA Anemometer WS-10U
12	VPA Anemometer WS-10V
13	VPA Anemometer WS-10W
15	VPA Anemometer WS-11U

VPA & Local Met (PCM #3)

Ch	Parameter
01	VPA Anemometer WS-11V
02	VPA Anemometer WS-11W
03	VPA Anemometer WS-12U
04	VPA Anemometer WS-12V
05	VPA Anemometer WS-12W
06	VPA Anemometer WS-13U
07	VPA Anemometer WS-13V
08	VPA Anemometer WS-13W
09	TSI X-Film 1X
10	TSI X-Film 1Y
11	TSI X-Film 2X
12	TSI X-Film 2Y
13	Sonic Anemometer U-Axis
14	Sonic Anemometer V-Axis
15	Sonic Anemometer W-Axis

Turbine (PCM #5)

Ch	Parameter
01	Low Speed Shaft Azimuth Angle
02	Yaw Bending Moment
03	Tower Bending North Dir.
04	Tower Bending Moment East Dir.
05	Yaw Angle
06	Generator Power
07	Low Speed Shaft Speed

Rotor (PCM #4)

Ch	Parameter
01	Flap Bending 90% "1FBM"
02	Flap Bending 85% "2FBM"
03	Flap Bending 85% "3FBM"
04	Flap Bending Root "11FMB"
05	Flap Bending 75% "5FBM"
06	Flap Bending 75% "6FBM"
07	Flap Bending 60% "7FBM"
08	Flap Bending 50% "8FBM"
09	Flap Bending 40% "9FBM"
10	Flap Bending Root "10FBM"
11	Flap Bending 70% "12FBM"
12	Edge Bending Moment 90% "1EBM"
13	Edge Bending Moment 85% "2EBM"
14	Edge Bending Moment 75% "3EBM"
15	Edge Bending Moment 60% "4EBM"
16	Edge Bending Moment 50% "5EBM"
17	Edge Bending Moment 40% "6EBM"
18	Edge Bending Moment Root "7EBM"
19	Edge Bending Moment 70% "8EBM"
20	Blade Torsion 85% "1BLDTQ"
21	Blade Torsion 75% "3BLDTQ"
22	Blade Torsion Root "5BLDTQ"
23	Low Speed Shaft Torque "1LSSBM"
24	Low Speed Shaft Bending X Dir. "2LSSBM"
25	Low Speed Shaft Bending Z Dir. "3LSSTQ"
26	Load Cell Channel
27	Pressure #1 100% chord span, trailing
28	Pressure #2 92% chord span, upper
29	Pressure #4 80% chord span, upper
30	Pressure #6 68% chord span, upper
31	Pressure #8 62% chord span, upper
32	Pressure #10 44% chord span, upper
33	Pressure #11 36% chord span, upper
34	Pressure #13 20% chord span, upper
35	Pressure #14 14% chord span, upper
36	Pressure #15 10% chord span, upper
37	Pressure #16 8% chord span, upper
38	Pressure #17 6% chord span, upper
39	Pressure #18 4% chord span, upper
40	Pressure #19 2% chord span, upper
41	Pressure #20 1% chord span, upper
42	Pressure #20A .5% chord span, leading
43	Pressure #21 0% chord span, leading
44	Pressure #21A .5% chord span, lower
45	Pressure #22 1% chord span, lower
46	Pressure #23 2% chord span, lower
47	Pressure #24 4% chord span, lower
48	Pressure #25 6% chord span, lower
49	Pressure #27 10% chord span, lower
50	Pressure #28 14% chord span, lower
51	Pressure #29 20% chord span, lower
52	Pressure #30 28% chord span, lower
53	Pressure #32 44% chord span, lower
54	Pressure #33 56% chord span, lower
55	Pressure #34 68% chord span, lower
56	Pressure #35 80% chord span, lower
57	Pressure #36 98% chord span, lower
58	Total Pressure Probe
59	Calibration Pressure
60	Absolute Reference Pressure
61	Pitch Angle
62	Angle of Attack Probe

WIND TUNNEL TESTS

Two wind tunnel test programs were conducted on the S809 airfoil used in the Combined Experiment. The first one was conducted to confirm that the airfoil performed according to design specifications, because the airfoil was designed using a computer code. A very accurate and smooth test model was used with more than 100 pressure taps. The Delft wind tunnel in Holland was used because of its extremely low turbulence level. The test matrix included steady-state data runs at Reynolds numbers from 1 to 3 million. Data from rough and smooth conditions were acquired, along with oil-film flow-visualization tests. These test results are considered the reference two-dimensional airfoil data set. All future wind tunnel data and rotating, three-dimensional pressure data will be compared to this set.

The second wind tunnel test was conducted at Ohio State University (OSU) in an open-circuit wind tunnel measuring 0.92 m x 1.53 m (3 ft x 5 ft). The objective of this test was to establish a credibility link between the Delft data, the test airfoil, and SERI instrumentation. At OSU, the wind tunnel test model used was fabricated in the same molds that were used to make the test blade. Pressure taps were located in exactly the same positions as those on the test blade, and the same pressure transducer was used in the rotating blade test and the wind tunnel. Data measured from the OSU wind tunnel were then compared with the data from the Delft wind tunnel. Some differences were found, as expected, and will be discussed in the following section. After the differences were documented, a credible basis was established for comparing three-dimensional pressure distributions with two-dimensional data.

Results

Figures 6 and 7 compare lift coefficients (C_l) with AOA ("Alpha" on the figures) for Delft wind tunnel data and OSU data. Figure 6 shows Delft data for the smooth condition. There is good agreement for Alpha less than 7°. When Alpha is greater than 7°, the OSU lift coefficients are lower than Delft coefficients by as much as 10% at $C_{l,max}$.

This difference could be caused by two factors. When pressure taps are lined up along the chord, as they were on the OSU model, the taps cause roughness, which in turn can cause premature transition of the boundary layer, adverse pressure gradients, and premature separation. The end result is that $C_{l,max}$ is lower. Another contributor could be the minimal number of pressure taps used in the OSU tests. The field tests will be limited to 32 pressure taps, so only 32 were used in the wind tunnel tests.

As mentioned earlier, the Delft tests included 108 pressure taps in staggered patterns. The pressure distributions are defined far more accurately because of the higher tap density. For example, Figure 8 shows comparable pressure distributions from Delft and OSU data. The laminar transition, which is well defined on upper and lower surfaces as a knee at 55% chord, is poorly defined by the sparsely distributed pressure taps on the OSU model. Figure 9 shows a very sharp pressure peak near the leading edge. The Delft model had 20 taps on upper and lower surfaces within the first 5% of the airfoil. The maximum number of taps on the OSU model and test blade was 9, all within the first 5% of the chord. Therefore, the Delft data indicate a more accurate definition of the pressure peak.

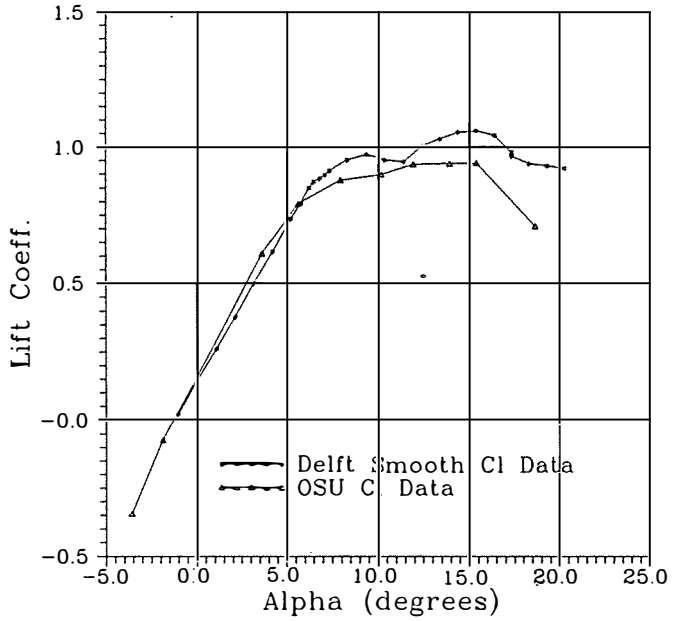

Fig. 6. Comparison of smooth lift curves for the Delft and OSU data

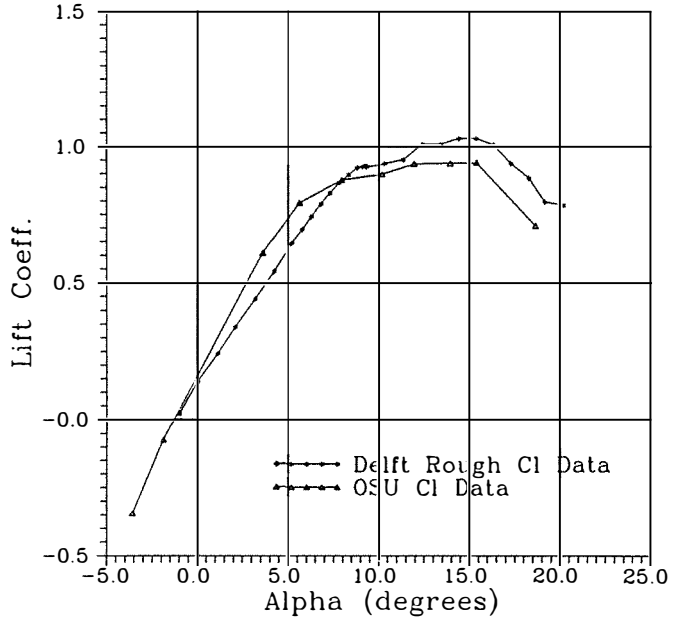

Fig. 7. Comparison of rough lift curves for the Delft and OSU data

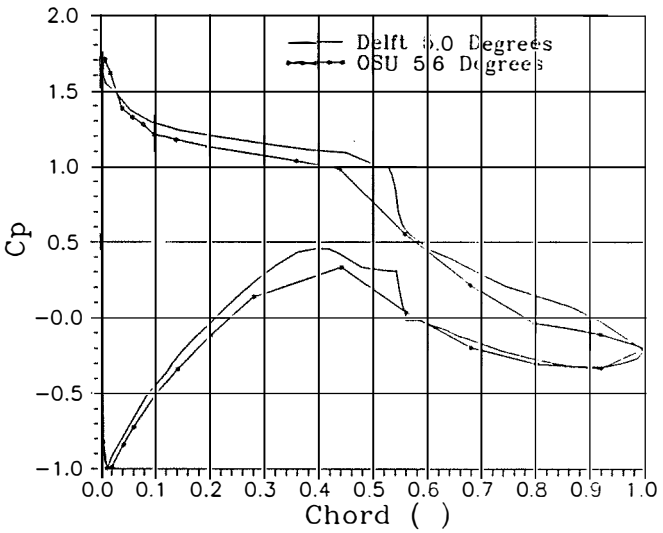

Fig. 8. Comparison of pressure distributions for the Delft and OSU data

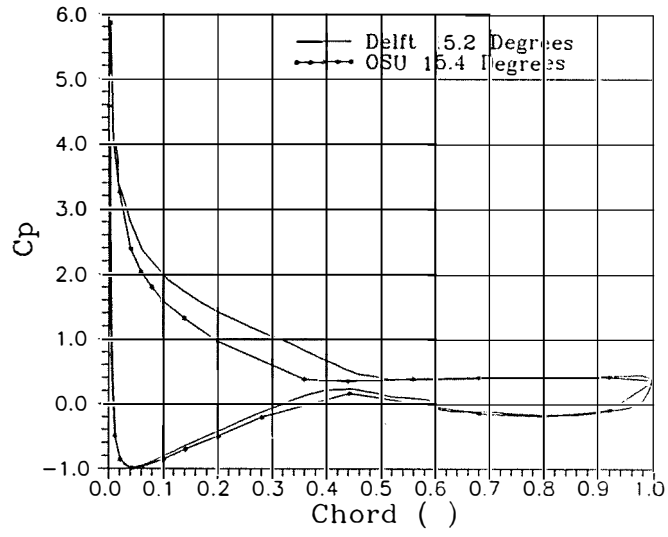

Fig. 9. Comparison of pressure distributions for the Delft and OSU data

An exact match was not expected. The goal of the comparison was to document these differences so that field data could be compared to Delft or OSU data, and rotational effects could easily be isolated from test setup and instrumentation effects. This has been accomplished.

There was good general agreement between lift curve slopes, α at $C_l = 0$, minimum coefficient of drag ($C_{d,min}$) (Figures 10 and 11), and pitching-moment coefficient (Figures 12 and 13). The general shape of the pressure distributions agrees also, with the exception of the effects of the taps (as described previously and shown in Figures 8 and 9).

PRELIMINARY FLOW VISUALIZATION RESULTS

As mentioned earlier, "mini tufts" were used as the primary flow-visualization tool. Cooperative tests involving Sandia National Laboratories were also conducted using liquid crystals (5) to investigate the boundary-layer mechanics. However, these results are mentioned only briefly in this report. Future reports will address the liquid-crystal results in detail (6).

Figures 14 through 17 were made by freezing a video frame using a Data Translation "Frame Grabber" to transfer the video image to a Compaq 386 computer, enhancing the image, then printing the enhanced image on

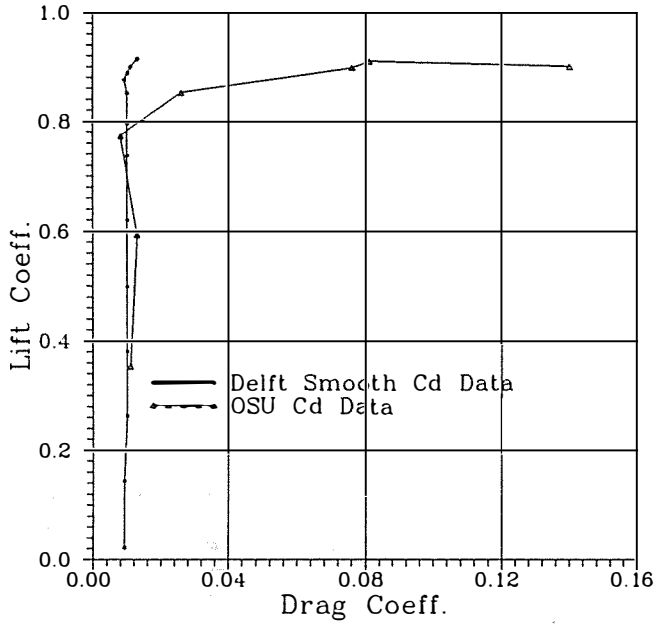

Fig. 10. Comparison of smooth drag polars for the Delft and OSU data

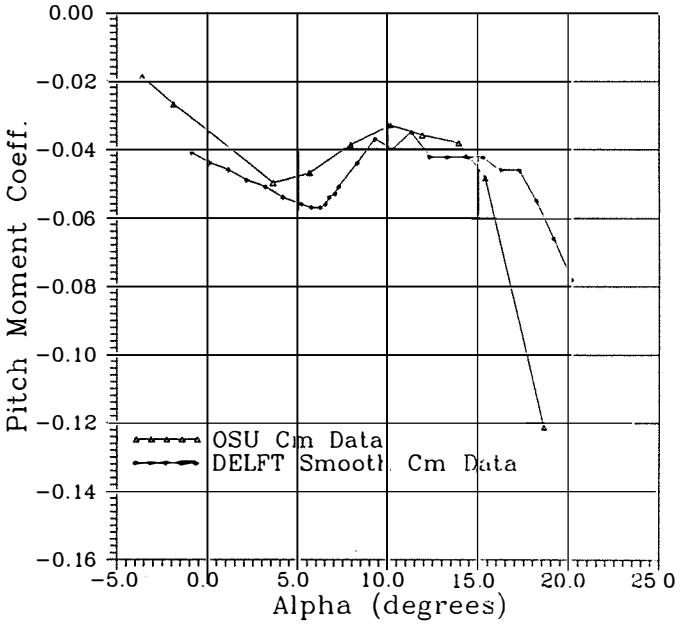

Fig. 12. Comparison of smooth pitching moments for the Delft and OSU data

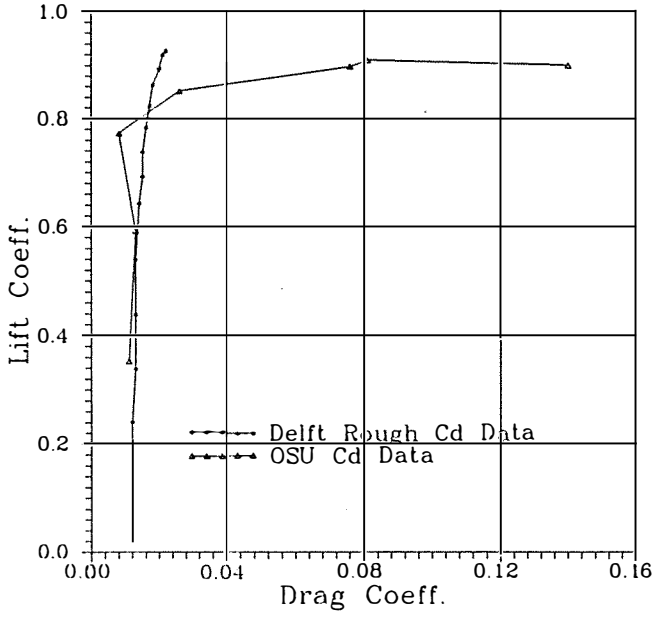

Fig. 11. Comparison of rough drag polars for the Delft and OSU data

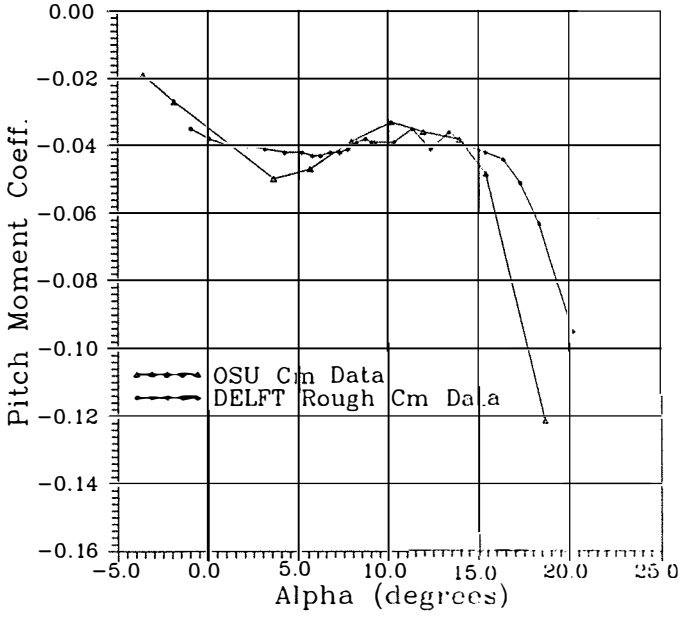

Fig. 13. Comparison of rough pitching moments for the Delft and OSU data

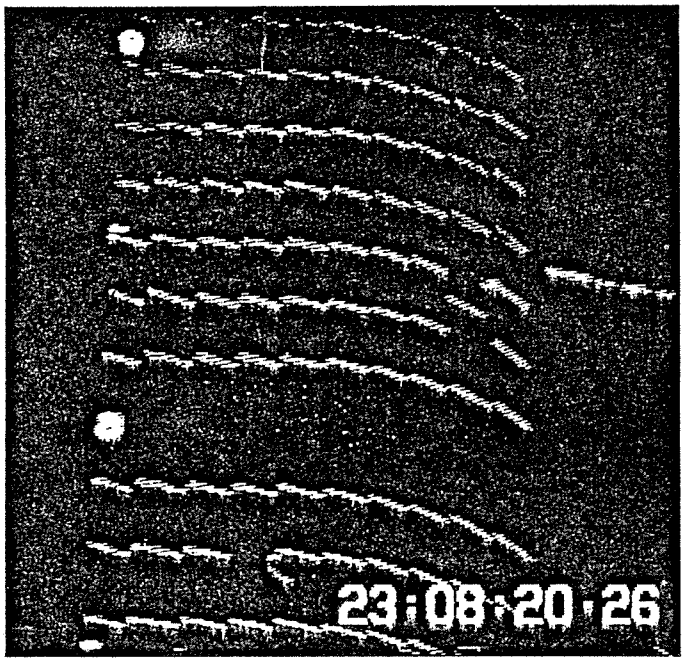

Fig. 14. Outboard tufts at low AOA

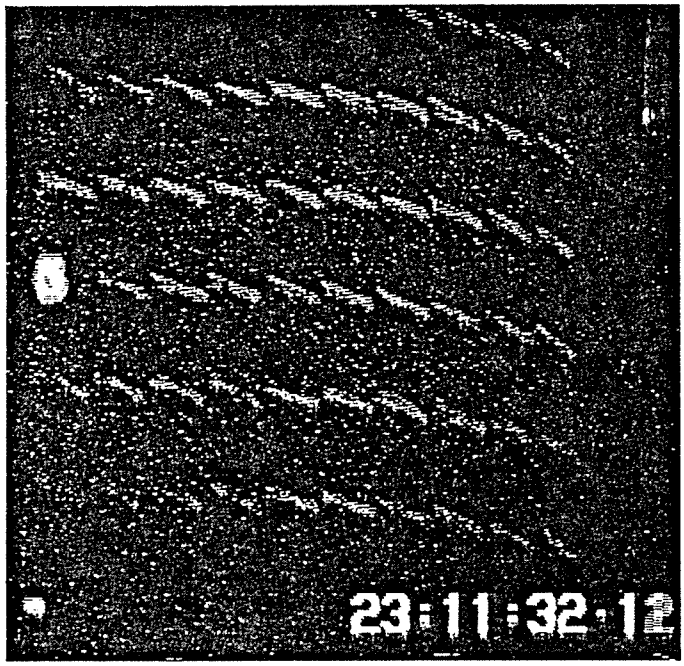

Fig. 15. Inboard tufts at low AOA

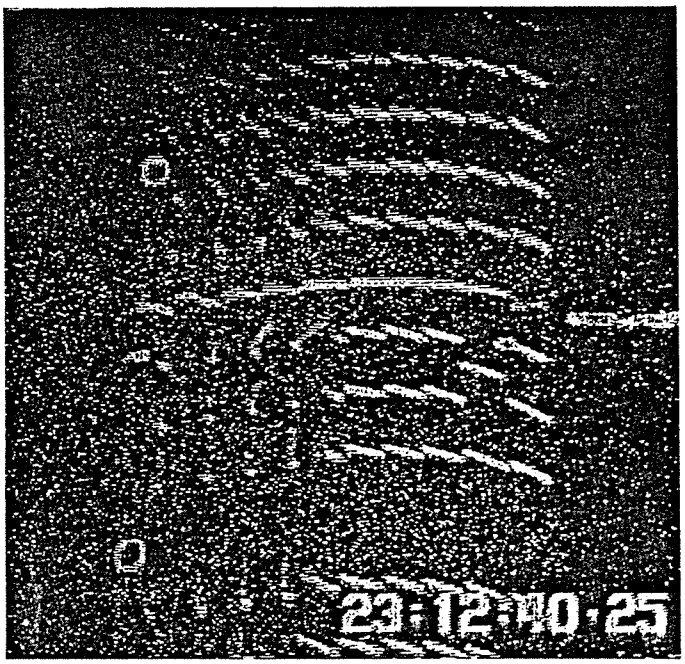

Fig. 16. Outboard tufts at high AOA

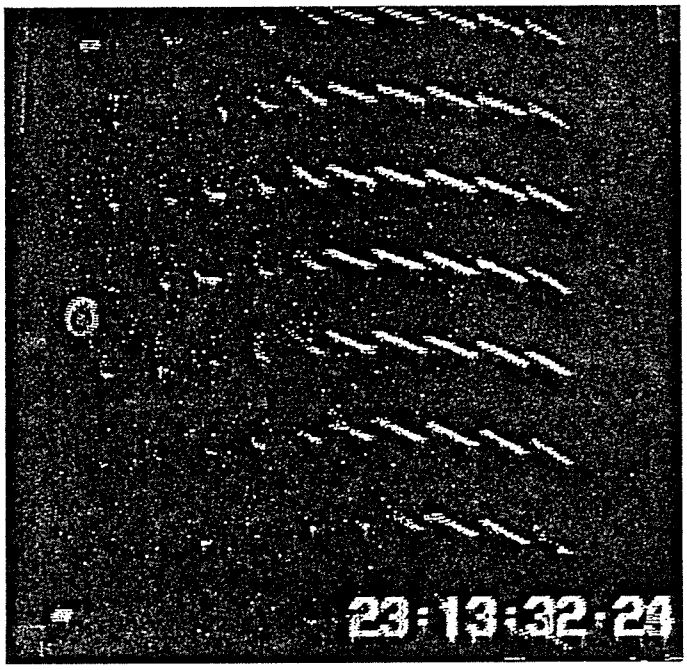

Fig. 17. Inboard tufts at high AOA

a laser printer. The videos were recorded at night, so the entire background was black. Because the blade itself was flat black, the only illuminated objects are the tufts. The blade spanwise location numbers attached to the trailing edge are also visible at the left edge of the figures. A video time-code stamp is visible at the bottom of each figure. The first row of tufts is attached at the 5% chord and, therefore, identifies the leading edge. The last row of tufts is trimmed flush with the trailing edge.

These images are poor reproductions; therefore, it is useful to know that when a tuft is engulfed by laminar flow it remains steady and presents a clear image to the video camera. When a tuft is engulfed in separated flow, it dances around rapidly and presents a blurred image, barely visible on the video recording. This problem was compounded by night testing because the darkness prevented using the camera's fast shutter. The shutter would normally freeze the image without blur, but it requires much more light than was avail-

able during night tests. Viewing the videos in motion, it is far easier to see the angles of the tufts than it is when freezing the frame and displaying it on a hard copy.

Figure 14 shows the blade span from 75% (bottom of the figure) to 90% (top of the figure). The AOA is near zero in this case, and the tufts are all steady and nearly aligned with the chord. Centrifugal force causes a slight deflection of the tufts toward the tip. The fourth tuft from the left in the second row from the bottom is stuck against the blade surface and should be neglected. This figure indicates that no significant spanwise flow is affecting the tuft angles.

Figure 15 shows the 45%-55% blade span for the same operating condition (low AOA, 7 m/s winds). Again, the flow over the airfoil is attached and steady. A very slight increase in the tuft angles can be seen. This should be expected because the local chordwise flow velocity is 55% of that in Figure 14 because of its inboard location. So, Figures 14 and 15 show no surprising or interesting results, except that no significant spanwise flow is detectable.

Figure 16 shows the same outboard blade section (78%-95%) at an AOA of 5°-10°. The flow from the leading edge to approximately 55% chord is attached and steady. The flow from 50% chord to the trailing edge is separated except at the 86% span, where an instrument probe extends forward from the leading edge along the chord line. The narrow band of turbulence caused by flow over the probe causes the flow over the aft surface to remain attached. This is not a surprising result. Vortex generators have been shown to keep flow attached on an airfoil by energizing the boundary layer and inhibiting adverse pressure gradients. What is surprising is that on either side of this "aerodynamic fence" the separation boundary location appears to be unaffected; that is, at both the 85% and 88% span, the separation boundary is located at 55% chord.

If the performance of spanwise sections were affected by neighboring sections, a deflection of the separation boundary, outboard of 86%, would have been expected. If spanwise flow in the separation region were influencing the location of the separation boundary location, attached flow behind the probe would have cut off this spanwise flow, and a discontinuity in the boundary location between 85% and 88% would have been visible. No such anomalies were visible.

This implies that, at least for this operating condition, adjacent blade stations can be considered to operate independently. This assumption is at the core of almost every HAWT performance and load analysis but has not been confirmed until now. Future tests will focus on this technique to confirm or disprove this basic assumption further.

By panning the video camera, inboard flow patterns at a section in the 55%-65% span could be recorded. Figure 17 shows such an image 52 s after that of Figure 16. The separation boundary at 65% span is still located at 55% chord, but inboard of the 60% span the boundary quickly sweeps toward the leading edge. Figure 18 shows, schematically, the separation boundary location throughout the entire blade for this moderate AOA operating condition.

Liquid crystals were used to visualize the boundary-layer surface shear-stress patterns on the airfoil as part of a cooperative program with Sandia National Laboratories. The purpose of these tests was to determine if the boundary-layer shear-stress patterns were modified by rotational effects. The S809 airfoil has a laminar separation bubble located at 58% chord at AOA = 0°, and it moves forward as AOA increases. Figure 19 maps the location of this bubble during the Delft wind tunnel tests. Figure 20 shows a liquid-crystal color and rivulet pattern at AOA = 0°-5°

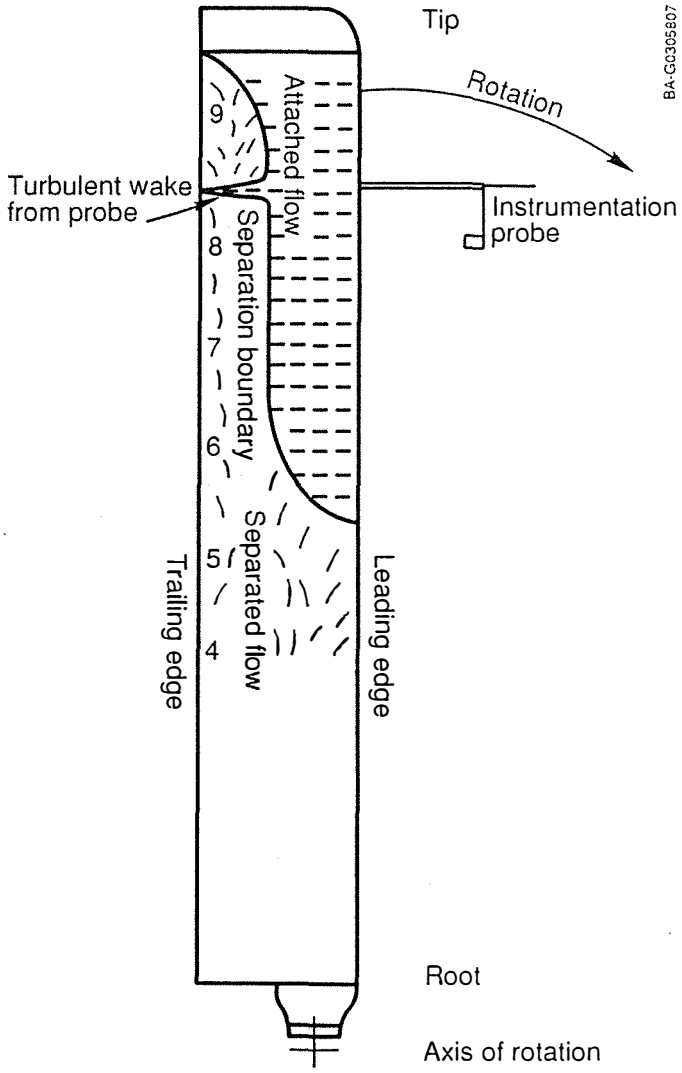

Fig. 18. Location of the separation boundary on the blade

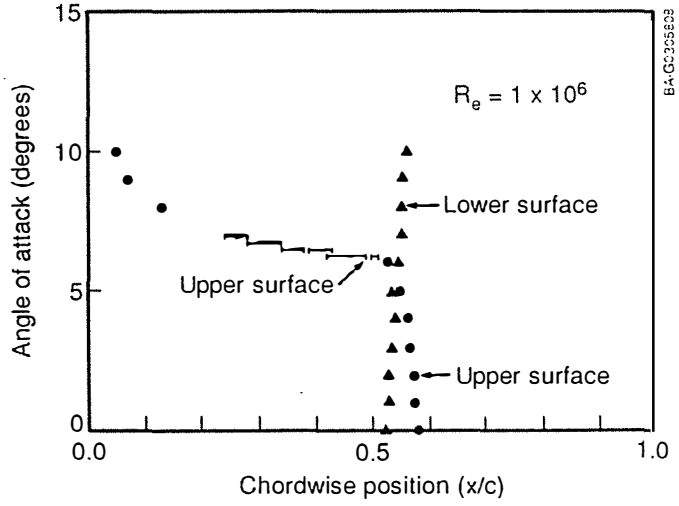

Fig. 19. Location of the boundary layer transition on the blade (Delft wind tunnel data)

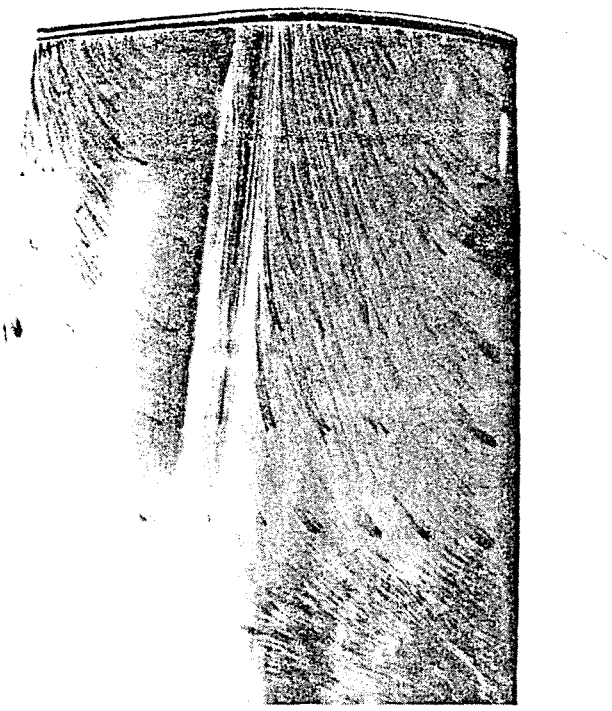

Fig. 20. Liquid crystal on the rotating blade

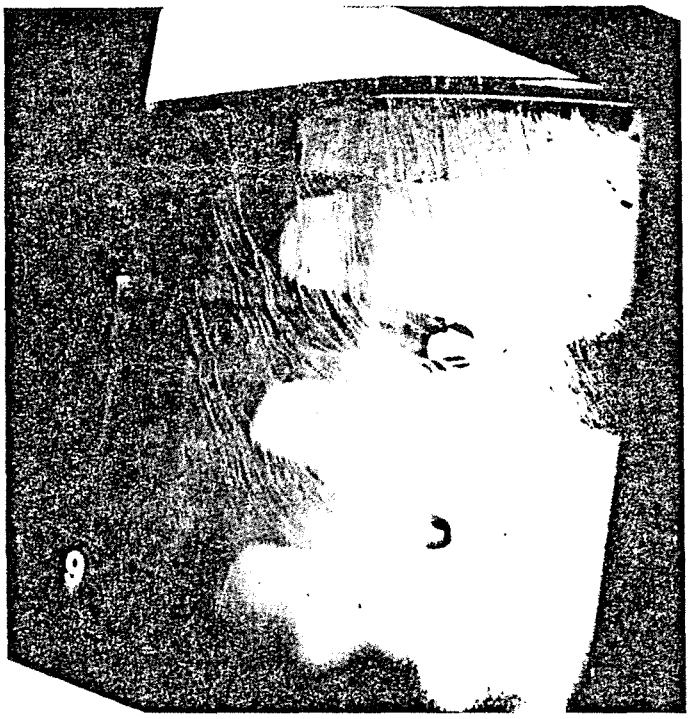

Fig. 21. Liquid crystal on the rotating blade with protuberances

that clearly identifies the location of this bubble at 55%-60% chord and confirms Delft wind tunnel measurements.

Figure 21 shows a similar test using liquid crystals, plus three protuberances mounted on the blade surface at AOA = 0°-5°. The first protuberance was a flat piece of aluminum, 6 mm wide and bent perpendicular to the blade surface. This tab was mounted at approximately 91% span and 30% chord. The next was a vortex generator mounted at 94% span and 30% chord. The third protuberance was a moth impact that occurred shortly after the run began. It is located at 97% span and 35% chord. All these protuberances show turbulent wakes extending toward the trailing edge. The turbulent wakes begin in the laminar flow region and extend straight through the bubble into the turbulent, attached flow region near the trailing edge. These wakes appear to be uninfluenced by any spanwise flow; this further supports the conclusion that at low to moderate AOA the flow appears to behave in a two-dimensional fashion.

PRELIMINARY PRESSURE MEASUREMENTS

Pressure-distribution data recorded to date covers wind speeds from near 0 m/s to 12 m/s. During "zero" wind conditions, data were collected by motoring the turbine. This technique was used to achieve nearly steady aerodynamic conditions for checking measurements with predictions. These comparisons will be used to validate the measurement procedure. After these comparisons are complete, high-wind-speed steady data (approaching stall) will be analyzed.

"Steady" stall or peak power performance has always been difficult to predict using available computer analysis. This operating condition is expected to yield the largest discrepancies between theory and test data. Unfortunately, no high-wind-speed/high-AOA data

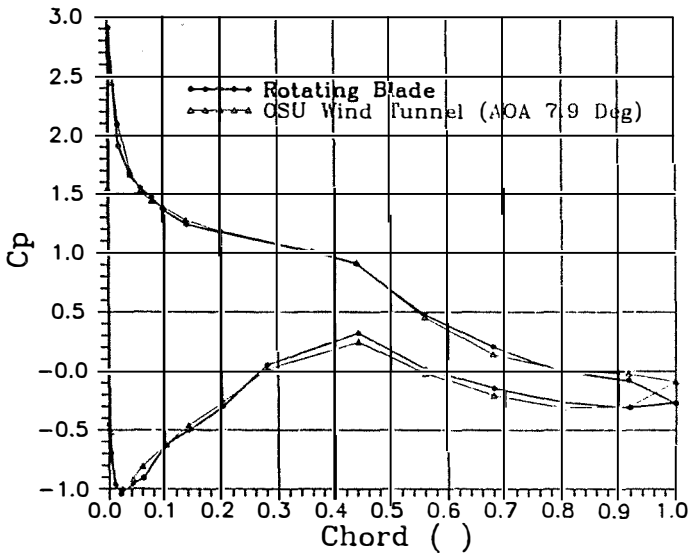

Fig. 22. Comparison of pressure distributions for the rotating blade and the wind tunnel

are available at this time. Low- to moderate-wind-speed preliminary data are available and are discussed in the following text.

Raw pressure tap data were normalized by measured dynamic pressure. A pressure probe, mounted on the blade and extending forward 0.68 m from the leading edge, was used to measure dynamic pressure. The data were sampled at 522 Hz per tap. No curve fitting has been performed on any of the data presented here, yet the distributions are relatively smooth.

Figure 22 shows two pressure distributions. One was taken from the OSU wind tunnel data base; the other

was taken from the rotating wind turbine blade. The AOA for the OSU data is known to be 7.9°. The rotating-data AOA is not available yet, but it is assumed to be similar because the two distributions match fairly well. This sample was selected for a preliminary comparison only and does not reflect a complete comparison of all operating conditions; still, it does imply that for moderate winds (low AOA), rotating airfoils perform much like they would in a wind tunnel.

Figure 23 shows a time sequence of upper surface pressures during a low-wind-speed condition. Each curve represents the average of two instantaneous samples for an effective sample rate of 104 Hz. The entire sequence is 0.85 s long, slightly more than one rotor revolution. Near the leading edge, the familiar pressure peak is obvious, as is the knee in the pressure recovery region near the 50% chord. This knee is obvious in both sets of wind tunnel data and is particularly sharp at moderate AOA because of the laminar separation bubble at this point. As AOA increases, this knee tends to smooth out at the bubble, becomes thinner, and moves forward on the airfoil.

Returning to the leading edge pressure peak, it is clear that the airfoil experiences dynamic AOA changes even in these moderate wind speeds. Levels of local pressure coefficients range from 1.0 to -3.0. A change in AOA from 3° to 8° would be required to cause this range of pressure peak change (in local pressure coefficient, C_p) in wind tunnel data. This change occurs over approximately 100 ms, toward the latter end of the sequence.

The last distribution shown in the sequence coincides with the blade entering the tower wake. It is clear from this sequence, and most sequences studied to date, that the tower wake has a dramatic effect on the pressure distributions. When the blade enters the tower wake, the AOA drops and causes the drop in pressure peak shown in the last curve of Figure 23. As the blade emerges from the tower wake, the lift is reestablished as quickly as it drops off. This momentary drop in aerodynamic load causes a drop in structural load, which can be seen in strain gage data (not shown in this report).

FUTURE WORK

Testing is not complete. High-wind-speed, high-AOA data are needed to study modifications to stall behavior on the rotating blade. A detailed analysis of pressure distributions and integrated aerodynamic force coefficients will be conducted. A very important area yet to be investigated is how these measured aerodynamic loads correlate with dynamic blade loads. This kind of investigation will help designers predict damaging fatigue loads more accurately. Studies will be conducted on how to reduce or avoid such loads.

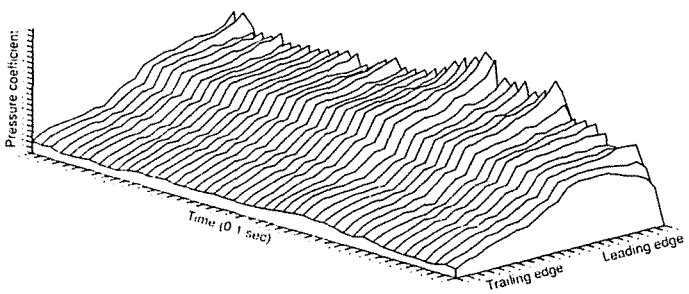

Fig. 23. Pressure distribution time sequence

Pitch control versus stall control of wind turbine power will be studied to see if dynamic loads can be relieved through aerodynamic stall regulation. Yawed operation will be studied to investigate the source of high dynamic loads and yaw stability.

In the area of inflow, vertical-plane-array data and atmospheric boundary layer data will be used to investigate which atmospheric conditions are most damaging and which are most productive. This work will help wind prospectors differentiate between potentially damaging sites and productive sites.

CONCLUSIONS

More testing in higher-wind-speed conditions is needed before major conclusions can be drawn about the three-dimensional affects on the stall behavior of a rotating wind turbine blade.

At low AOA, this S809 airfoil appears to behave much like it would in two-dimensional wind-tunnel-type flow.

It appears that the aerodynamic environment, in which the wind turbine blade operates, is unsteady.

ACKNOWLEDGMENTS

Many people at SERI and outside of SERI have contributed to this work. Not all can be mentioned here, but credit to Dave Simms and Mike Jenks should be given for the major contributions they have made in the area of software development and technical support. As mentioned earlier, Dan Reda of Sandia National Laboratories provided the liquid-crystal expertise in the boundary-layer tests. Bob Akins of Washington and Lee University, and Craig Hansen of the University of Utah, also provided valuable advice and guidance. Also, Al Eggers has been very helpful in his theoretical contributions to the test program.

REFERENCES

1. Tangler, J. L. and Somers, D. M., "Status of the Special-Purpose Airfoil Families," Proceedings of Windpower '87, SERI CP-217-3315, American Wind Energy Association, Arlington, Virginia, 1988.

2. Irwin, H. P. H. H., Cooper, K. R., and Girard, R., "Correction of Distortion Effects Caused by Tubing Systems in Measurements of Fluctuating Pressures," Journal of Industrial Aerodynamics, Vol. 5, 1979, pp. 93-107.

3. Rae, W. H. Jr. and Pope, A., Low-Speed Wind Tunnel Testing Second Edition, John Wiley & Sons, New York, 1984, p. 133.

4. Lenschow, D. H., "Vanes for Sensing Incidence Angles of the Air from an Aircraft," Journal of Applied Meterology, Vol. 10, No. 6, 1971, pp. 1339-1343.

5. Reda, D. C., "Liquid Crystals for Unsteady Surface Shear Stress Visualization," AIAA 88-3841CP, First National Fluid Dynamics Congress, Cincinnati, Ohio, July 25-28, 1988.

6. Reda, D. C. and Butterfield, C. P., "Liquid-Crystal/Shear Stress Visualization on a HAWT," Proceedings of Eighth ASME Wind Energy Symposium, January 1989.